CrossMark

RESEARCH PAPER

Effect of absolute pressure on flow through a textured hydrophobic microchannel

D. Dilip[1] · M. S. Bobji[1] · Raghuraman N. Govardhan[1]

Abstract The potential of textured hydrophobic surfaces to provide substantial drag reduction has been attributed to the presence of air bubbles trapped on the surface cavities. In this paper, we present results on water flow past a textured hydrophobic surface, while systematically varying the absolute pressure close to the surface. Trapped air bubbles on the surface are directly visualized, along with simultaneous pressure drop measurements across the surface in a microchannel configuration. We find that varying the absolute pressure within the channel greatly influences the trapped air bubble behavior, causing a consequent effect on the pressure drop (drag). When the absolute pressure within the channel is maintained below atmospheric pressure, we find that the air bubbles grow in size, merge and eventually detach from the surface. This growth and subsequent merging of the air bubbles leads to a substantial increase in the pressure drop. On the other hand, a pressure above the atmospheric pressure within the channel leads to gradual shrinkage and eventual disappearance of trapped air bubbles. We find that in this case, air bubbles do cause reduction in the pressure drop with the minimum pressure drop (or maximum drag reduction) occurring when the bubbles are flush with the surface. These results show that the trapped air bubble dynamics and the pressure drop across a textured hydrophobic microchannel are very significantly dependent on the absolute pressure within the channel. The results obtained hold important implications toward achieving sustained drag reduction in microfluidic applications.

Keywords Textured hydrophobic surface · Trapped air bubbles · Pressure drop · Drag reduction

✉ Raghuraman N. Govardhan
raghu@mecheng.iisc.ernet.in

[1] Department of Mechanical Engineering, Indian Institute of Science, Bangalore 560 012, India

1 Introduction

Microfluidic devices have evoked considerable interest in recent years because of their immense potential to be used in a wide variety of applications. Microfluidic passages, owing to their large surface area to volume ratio, exhibit large pressure drop (drag) as flow is induced through them. Textured hydrophobic surfaces characterized by microscale/nanoscale roughness and low surface energy have been demonstrated to be capable of delivering substantial drag reduction in microfluidic applications (Watanabe et al. 1999; Tretheway and Meinhart 2002; Choi et al. 2003, 2006; Ou et al. 2004; Gogte et al. 2005; Truesdell et al. 2006; Lee et al. 2008; Govardhan et al. 2009; Woolford et al. 2009; Yamada et al. 2011). Naturally occurring textured hydrophobic surfaces have attracted enormous attention (Parker and Lawrence 2001; Hu et al. 2003; Gao and Jiang 2004; Cong et al. 2004; Cheng and Rodak 2005; Koch and Barthlott 2009), and the development of specially textured hydrophobic surfaces by mimicking nature has been a topic of active research and review (Shirtcliffe et al. 2010; Samaha et al. 2012c; Celia et al. 2013). Such biomimetic surfaces lend themselves to be suitable for many applications including drag reduction, underwater respiration (Shirtcliffe et al. 2006; Flynn and Bush 2008) and antifouling (Bixler et al. 2014). A review of drag reduction studies on textured hydrophobic surfaces has recently been carried out by Rothstein (2010). Some of these studies

done over a variety of patterned surfaces have reported large reductions in drag of the order of 30–40 % (Ou et al. 2004; Govardhan et al. 2009).

Many of the drag reduction studies carried out recently have been made using micro-posts/pillars (Ou et al. 2004), ridges (Ou and Rothstein 2005), micron-sized holes (Dilip et al. 2014) and surfaces with random surface features (Govardhan et al. 2009; Samaha et al. 2012b). The drag reduction obtained on such surfaces has been attributed to the presence of trapped air at the solid–liquid interface (Ou et al. 2004; Govardhan et al. 2009; Sheng and Zhang 2011; Samaha et al. 2012a, b; Dilip et al. 2014). Theoretical studies indicate that for achieving large reduction in drag, large shear-free area in conjunction with large air fraction is required (Lauga and Stone 2003; Teo and Khoo 2009). Tiny air bubbles of diameter less than a micron can, however, exist on suitable recesses in hydrophobic surfaces indefinitely (Liebermann 1957), although the smaller bubble size limits the amount of drag reduction to insignificant values (Lauga and Stone 2003). Surfaces with large features (>30 microns), capable of trapping large amounts of air on their cavities, have been shown (Ou et al. 2004; Govardhan et al. 2009) to deliver substantially higher drag reduction than their smoother counterparts. Govardhan et al. (2009) found that that the drag reduction achievable from textured hydrophobic surfaces is time-dependent and diminishes over time. This is because the trapped air gradually dissolves into the surrounding water and causes the surface to undergo a wetting transition from the favorable Cassie state to the unfavorable Wenzel state (Samaha et al. 2012a, b, d; Dilip et al. 2014). Recently, a number of studies have focused on the longevity of superhydrophobicity and the factors affecting the Cassie–Wenzel transition (Emami et al. 2013; Lv et al. 2014, 2015; Piao and Park 2015; Søgaard et al. 2014; Hemeda et al. 2014; Hemeda and Tafreshi 2014; Checco et al. 2014; Hensel et al. 2014; Xu et al. 2014; Bormashenko 2015). The dissolution of trapped air into water caused by the adverse concentration gradient across the air–water interface is thought to be the reason for the gradual disappearance of air pockets and thus the relatively short time over which drag reduction is actually achieved (Govardhan et al. 2009; Samaha et al. 2012b, d; Dilip et al. 2014). Hence, the air-retaining capability of the surface is important as it determines the longevity of superhydrophobicity.

Bobji et al. (2009) studied the air-retaining characteristics of hydrophobic surfaces with different surface textures under hydrostatic conditions and found that surfaces with blind holes are the most effective in trapping air and sustaining it. Such a surface is capable of trapping and confining large amounts of air inside the holes, which enables them to sustain the Cassie state for longer periods of time. In addition to the kind of texture used, the sustainability of

the Cassie state is also dependent on pressure (Bobji et al. 2009; Checco et al. 2014; Hensel et al. 2014; Lv et al. 2014; Søgaard et al. 2014; Xu et al. 2014; Piao and Park 2015), with higher pressures causing an early wetting transition. Poetes et al. (2010) observed that the lifetime of plastron layer on super hydrophobic surface undergoes rapid decay with increasing hydrostatic pressure. The effect of hydrostatic pressure on the wetting transition was also studied by Samaha et al. (2012b, d) who showed that beyond a certain "terminal pressure," wetting transition starts to occur resulting in reduced drag reduction and its sustainability in flow situations. In flow situations, in addition to effects of pressure, convective effects caused by the flow also accelerates the air removal from the cavities, which would cause the bubbles to disappear more rapidly. At larger flow rates, the stronger convection causes the entrapped air bubbles to dissolve into water at a higher rate, resulting in reduced longevity of superhydrophobicity (Samaha et al. 2012b). In the case of a hierarchical superhydrophobic surface consisting of dual-level topography, reversible switching between states has recently been shown by varying the pressure (Verho et al. 2012). In our earlier work (Dilip et al. 2014), we have shown that varying the absolute pressure can change the solubility of air in water and can thus help maintain the "Cassie" state on a textured hydrophobic surface. In the present work, we systematically vary the absolute pressure within a microchannel made of a textured hydrophobic surface and report on the pressure drop across the channel along with simultaneous visualizations of the trapped air bubbles on the surface. We show that by varying the absolute pressure, the rate of growth/decay of the trapped air bubbles can be controlled, which has large effects on the pressure drop.

In this paper, we present our experimental study on flow past a textured hydrophobic surface containing a regular array of blind holes to trap air bubbles. The surface is mounted inside a microchannel configuration, and the absolute pressure within the channel is systematically varied. Since the water is initially saturated with air at atmospheric pressure, a pressure above atmospheric pressure results in water flowing inside the channel being undersaturated. On the other hand, a lower pressure resulted in a supersaturated solution. In all cases, the trapped air bubbles on the surface are visualized along with simultaneous measurements of the pressure drop across the channel. To the best of our knowledge, there have been no prior systematic experiments on the flow through a textured hydrophobic channel, where the absolute pressure has both been increased and reduced, with simultaneous measurements of the pressure drop and visualization of the entrapped air bubbles on the surface. We show in the present work that the absolute pressure within the channel, by controlling the saturation level of air in water, can substantially alter both the bubble

dynamics of the entrapped air pockets on the surface and the pressure drop through the channel.

2 Experimental methods

A regular array of blind holes was generated on a smooth brass sheet of dimensions 100 mm × 30 mm × 0.8 mm by the process of photo-etching (Dilip et al. 2014). The brass metal sheet was laminated on one side by an ultraviolet light-sensitive photoresist and placed closely in contact under a photomask with the negative of the desired pattern printed on it. When UV light is allowed to fall on it, the exposed areas get hardened. The unexposed resist was then washed away leaving the areas to be etched unprotected. The metal surface was then exposed to a heated solution of cupric chloride in deionized water for a required amount of time, to etch away the unprotected metal, thereby delivering the required pattern.

The brass surface containing regular array of holes obtained after the etching process is shown in Fig. 1a. The characterization of the surface was done using a 3D non-contact optical profilometer (Veeco Instruments Inc.) with the measured 3D surface shown in Fig. 1b. The diameter of the hole was found to be close to 300 μm, depth 160 μm and pitch 370 μm, with variations in these dimensions being less than about 10 μm across the 100 mm × 30 mm

surface. The surface generated was originally hydrophilic and was made hydrophobic by chemical modification of the surface. For this, the surface was first cleaned with acetone and immersed in a 50 mM solution of 1-dodecanethiol in ethanol for 2 h for the formation of a self-assembled monolayer (Bobji et al. 2011; Pan et al. 2008; Dilip et al. 2014). The surface was then taken out and dried in an oven at 60 °C. Figure 1c shows the image of a water droplet on the surface obtained using an optical microscope, from which the contact angle was found to be 125°.

The textured hydrophobic surface was then mounted in a microchannel so that it formed a side wall of the channel (Fig. 2a). The other side wall of the channel was made of hydrophilic flat transparent glass to facilitate visualization of the textured surface. The channel cross section had a large aspect ratio of 30, the width of the channel being 1 mm, corresponding to the separation between the textured surface and the flat glass, and the vertical dimension being 30 mm. The channel width of 1 mm was chosen as widths of less than 1 mm resulted in bubbles growing and touching the other wall before bubble detachment for the given experimental conditions. The water used in the experiments was exposed to atmospheric air in a large tank for about 12 h prior to experiments and to enable air from the atmosphere to be dissolved in it. Prior to experiments, the water was tested with a dissolved oxygen meter (Hanna Instruments Model HI 9146) to ensure that is was
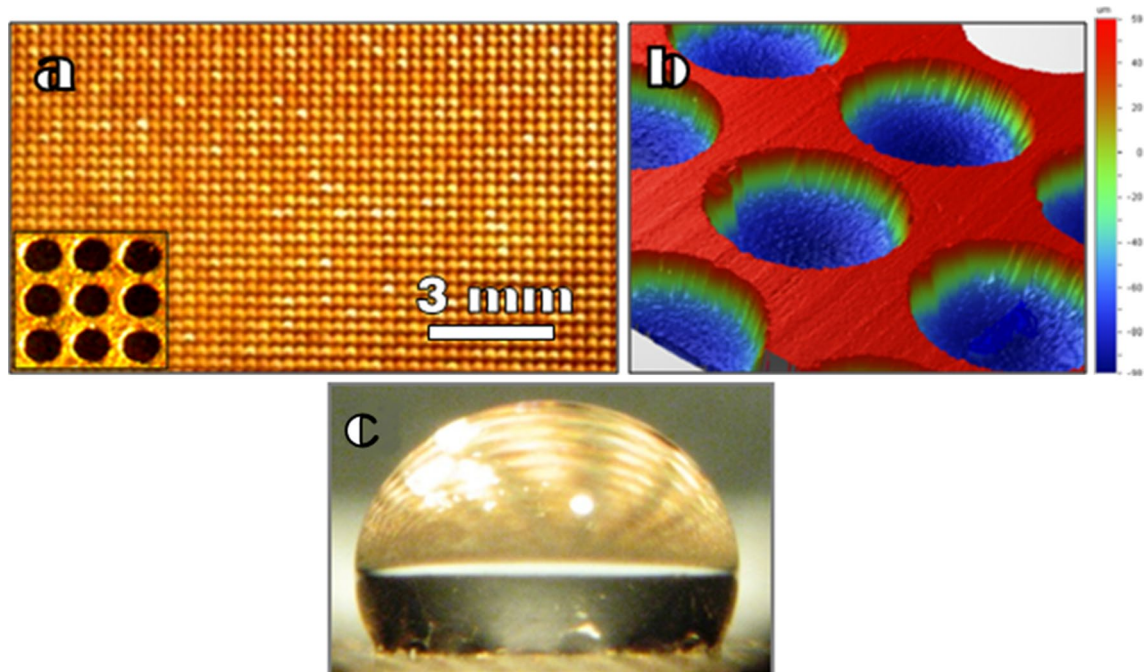

Fig. 1 **a** Optical picture of the brass surface patterned with a regular array of *blind holes*. **b** Contours of the *vertical* height, showing the *holes*, measured using a 3D profilometer. **c** Image of a water drop on the SAM-coated surface, showing the apparent contact angle of a water drop of about 125°

nearly saturated with air at atmospheric pressure. The water temperature during the experiments was close to 23 °C. In each case, just before the experiment, the channel was first dried and flushed with dry nitrogen for about 30 min, prior to the channel being filled slowly with water, such that air is trapped inside the holes, thus forming a bubble mattress over a large area. Water flow was driven through the channel by simple gravity flow from a large tank in which the water level was maintained constant to provide a fixed discharge. The absolute pressure within the microchannel was varied by varying the channel's vertical location with respect to the inlet tank water level. Pressures lower than atmospheric pressure were obtained within the channel by using the "siphon effect" created by placing the channel above the inlet tank level and discharging the water into atmospheric pressure at a lower level than that of the inlet tank level and the channel.

The air bubbles trapped on the surface were directly visualized using an optical microscope (Olympus LG-PS2) from the side as shown in the schematic (Fig. 2a) with diffused lighting from a halogen lamp Olympus (model no. SZX12). A camera attached to the optical microscope was used to record images of the trapped air bubbles at regular intervals of time. From analysis of these images, the trapped air bubble diameters could be obtained as a function of time. For larger viewing areas, we also used the principle of total internal reflection (TIR) of light at the water–air interface to detect the presence or absence of air within the holes. This technique has been successfully demonstrated previously by Govardhan et al. (2009), Bobji et al. (2009) and Larmour et al. (2007). The critical angle required for total internal reflection is given by $\theta_c = \sin^{-1}(1/\mu)$, where μ is the refractive index of water. A collimated beam of light incident on the surface at an angle greater than this critical angle undergoes total internal reflection at the trapped

Fig. 2 **a** Schematic of the microchannel setup. One of the walls of the channel is fitted with a textured hydrophobic surface. A transparent hydrophilic glass forms the other wall of the channel to facilitate visualization of air bubbles using an optical microscope. **b** Schematic illustrating the setup for visualizing the entrapped air pockets on the textured surface using total internal reflection. The light beam is incident at an angle greater than the critical angle required so that light gets totally internally reflected at the water–air interface
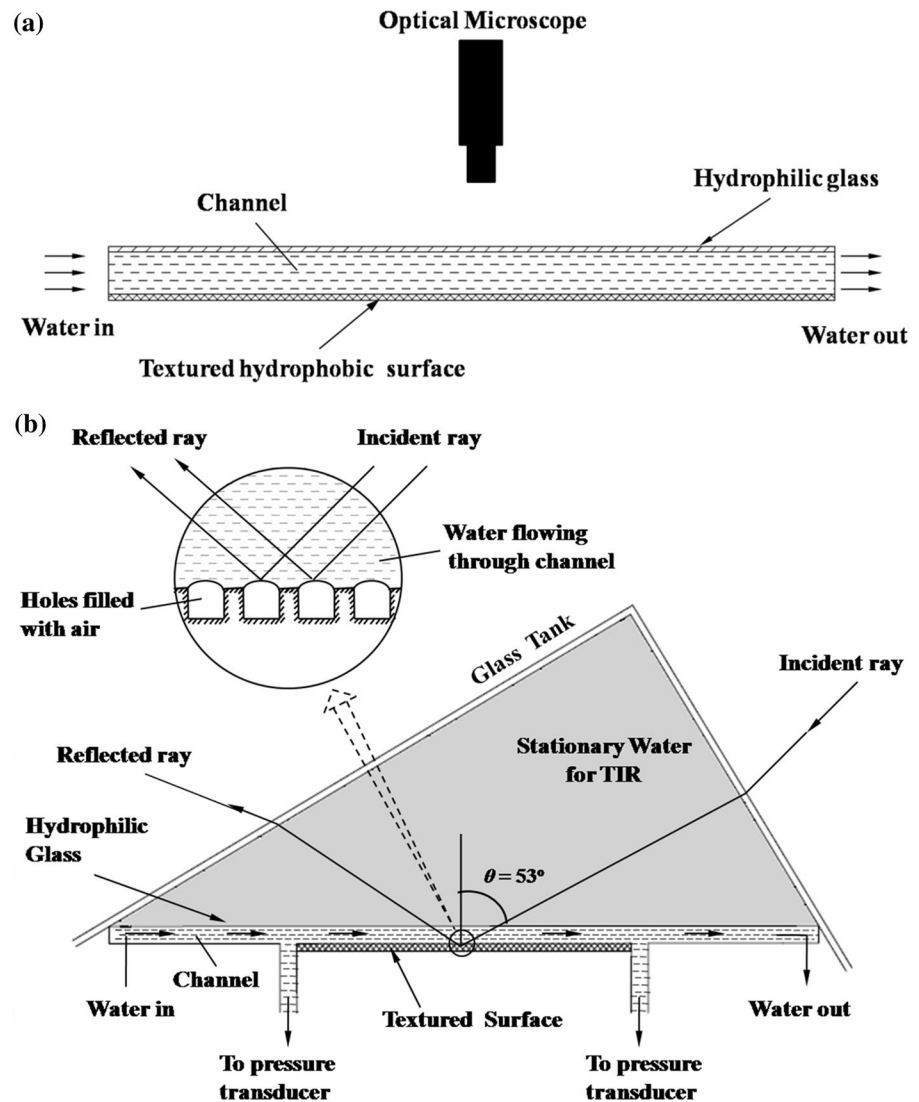
air pockets. The schematic of this TIR visualization setup is shown in Fig. 2b.

Pressure drop was measured using a differential pressure transmitter (Dwyer, Model 655A 316) across the streamwise length of the channel along with simultaneous visualization of trapped air bubbles to study the effect of the bubble mattress on drag. Flow rate was measured accurately by filling a beaker with water for a known length of time and measuring the weight of water with a precision digital balance. Pressure drop (ΔP) measurements were first done at various flow rates with the holes completely filled with water, i.e., in Wenzel state. This was used as the reference pressure drop in our experiments, and the measured values as a function of flow rate are shown in Fig. 3 from a set of about three runs. The pressure drop shows a linear variation with flow rate as expected at low Reynolds numbers within the laminar flow regime. All pressure drop measurements shown with trapped air later in the paper (ΔP) are normalized by the reference pressure drop (ΔP_o) shown in Fig. 3, for the corresponding flow rate (Q). The best fit line in Fig. 3 gives a channel width of 1.04 mm, which is slightly higher than 1 mm probably because of the "roughness" of the surface.

It should also be noted here that the absolute pressure within the channel ($P_{channel}$) referred to throughout the paper is the absolute pressure midway between the two pressure ports used to measure the pressure drop (ΔP). Further, the pressure drop (ΔP) values in our experiments are typically of the order of a few hundred Pa, as shown in Fig. 3, while the absolute pressure variations ($P_{channel} - P_{atm}$) that we shall present in the work will be of the order of a few thousand Pa, both below and above atmospheric pressure.

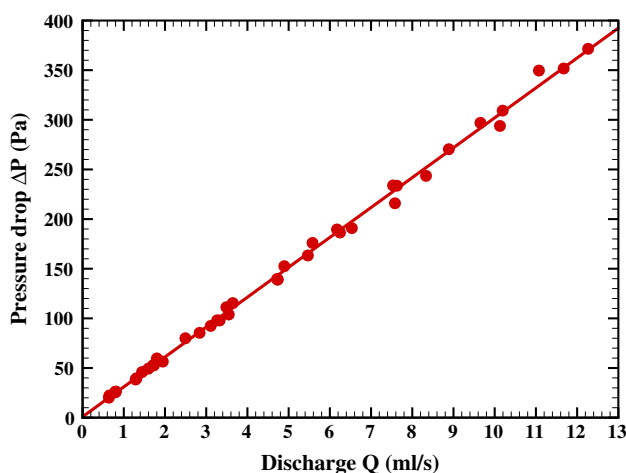**Fig. 3** Pressure drop measurements for the microchannel with no trapped air on the textured surface. The pressure drop (ΔP) shows a linear variation with flow rate (Q) as expected in the laminar regime

# 3 Pressures within the channel below atmospheric pressure ($P_{channel} < P_{atm}$)

In this section, we study the effect of flow over the bubble mattress when the absolute pressure inside the channel is lower than the atmospheric pressure. When water saturated with air enters the microchannel where the absolute pressure is lower than atmospheric pressure ($P_{channel} < P_{atm}$), due to reduced solubility, the water becomes supersaturated with air. This will lead to growth of bubbles trapped on the hydrophobic surface. First, we present the visualization of the bubble dynamics followed by pressure drop measurements.

Figure 4 shows the time sequence of images of the bubbles at a pressure of 1100 Pa below atmospheric and at a flow rate of 5 ml/s through the channel. For each image, a corresponding schematic is also shown to illustrate the water–air interface at that instant. When water is filled slowly inside the channel, air bubbles get trapped on the holes in the surface (Fig. 4a). As the supersaturated water flows over the bubbles, they grow in size more or less uniformly as shown in Fig. 4b, c. When the bubble diameter reaches a value equal to the pitch of the holes on the surface, they start to merge with adjacent bubbles as shown in Fig. 4d. This merging is not uniform and occurs randomly at various sites along the surface, probably driven by local inhomogeneities on the surface. These merged bubbles further grow bigger with time and eventually detach from the surface leaving nuclei of bubbles inside the holes (Fig. 4e). With time, these nuclei of bubbles also grow in size, merge and detach, and the cycle repeats indefinitely (Fig. 4f). The cycle of bubble growth, merging and detachment is highlighted by the corresponding schematics (a–f) also shown in Fig. 4. An example video showing growth, merging and detachment of bubbles for $P_{channel} < P_{atm}$ is shown in Online Resource 1.

From the images, such as those in Fig. 4, the diameter of the air bubbles in the streamwise direction (D) was measured. Figure 5 shows the variation of the measured diameter (D) of the bubbles normalized by the hole diameter (D_h) for three different channel pressures ($P_{channel}$) of 1100, 2950 and 5880 Pa below atmospheric pressure. The actual pressure values in the channel are lower as we go from (a) to (c). One can see in each case that there is a gradual growth of the bubble, as in the images in Fig. 4a–c, sudden increases in size related to bubble merger, as shown in Fig. 4d, and also sudden decreases caused due to bubble detachment, as shown in Fig. 4e. This cycle of gradual bubble growth, merger of adjacent bubbles and bubble detachment is seen to repeat in each case and is qualitatively similar at all pressures. There is, however, a clear difference in the time period for a cycle, as the pressure is lowered from

Fig. 4 Time sequence of images visualizing trapped air bubbles on a hydrophobic surface with *blind holes*. The pressure in the channel ($P_{channel}$) is maintained at 1100 Pa below atmospheric pressure. The flow rate is 5 ml/s. With time, the air bubbles grow, merge and eventually detach from the surface leaving smaller bubbles in the holes. The times after immersion are **a** $t = 0$ min, **b** $t = 30$ min, **c** $t = 45$ min, **d** $t = 50$ min, **e** $t = 55$ min, and **f** $t = 120$ min. The schematics shown indicate the air–water interface corresponding to each of the time sequence of images
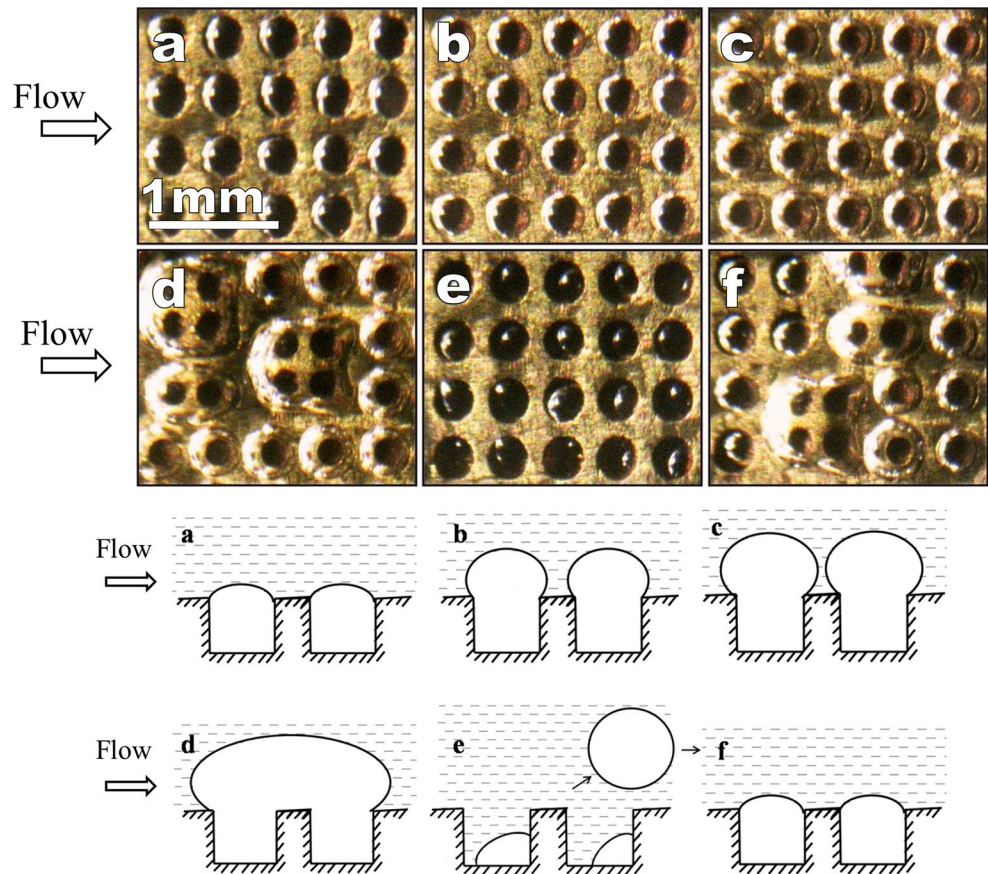
(a) to (c). In (a), the time period for a cycle is about 40 min for a pressure of 1100 Pa and decreases to about 15 min for a pressure of 5880 Pa, both pressure values being the magnitude below atmospheric pressure. At the lower pressures, the growth rate of the bubble is higher, and this leads to a smaller time taken for a cycle to repeat.

The rate of growth of the bubble is also significantly affected by the flow rate. Time traces of the bubble diameter at four different flow rates through the channel, while maintaining the pressure at 1100 Pa below the atmospheric pressure, are shown in Fig. 6, the flow rate being increased from (a) to (d). It is apparent from the figures that the process of growth and detachment of the air bubble is qualitatively the same in all cases. There are, however, two significant differences. Firstly, there is a significant increase in the growth rate of bubbles with flow rate. This can be seen by the decrease, for example, in the time period of a cycle of bubble growth, merger and detachment, which is about 40 min in (a) at 5 ml/s, and decreases to about 2 min at the highest flow rate in (d) of 28 ml/s. This may be compared to the convective effect of the flow on the decay of trapped air pockets at higher pressures reported earlier (Poetes et al. 2010; Samaha et al. 2012a, b, c, d; Dilip et al. 2014). In those cases, the higher pressures resulted in decay of the trapped air bubbles with time, which was further enhanced by convective effects. Here, at low pressures, the growth of the trapped air bubbles is found to be enhanced by convective effects.

Apart from the increased growth rate of the bubbles, there is also a clear difference in the detachment diameter of the bubble (D_d). As the flow rate increases, there is a larger drag force on the bubble, and hence, the detachment diameter (D_d) of the bubble is reduced. At lower flow rates, the detachment diameter is quite large and hence up to two mergers, as seen by two sudden rises in bubble diameter, may be seen in Fig. 6a, b. As the flow rate is further increased, the detachment diameter keeps getting reduced, and only one merger is shown in Fig. 6c and none in Fig. 6d, as the detachment diameter is in this case smaller than the bubble size after merger. In general, occurrence of bubble merger is dependent on the pitch to diameter ratio (P_h/D_h) of the holes and the detachment diameter (D_d) of the bubble at a given flow rate, with the probability of merger being larger for small (P_h/D_h) ratios, and being nearly absent if (P_h/D_h) ratios are sufficiently large. In addition, the width of the channel can also influence merging, especially if the bubbles grow and hit the opposite wall, although this did not occur in the experiments reported here.
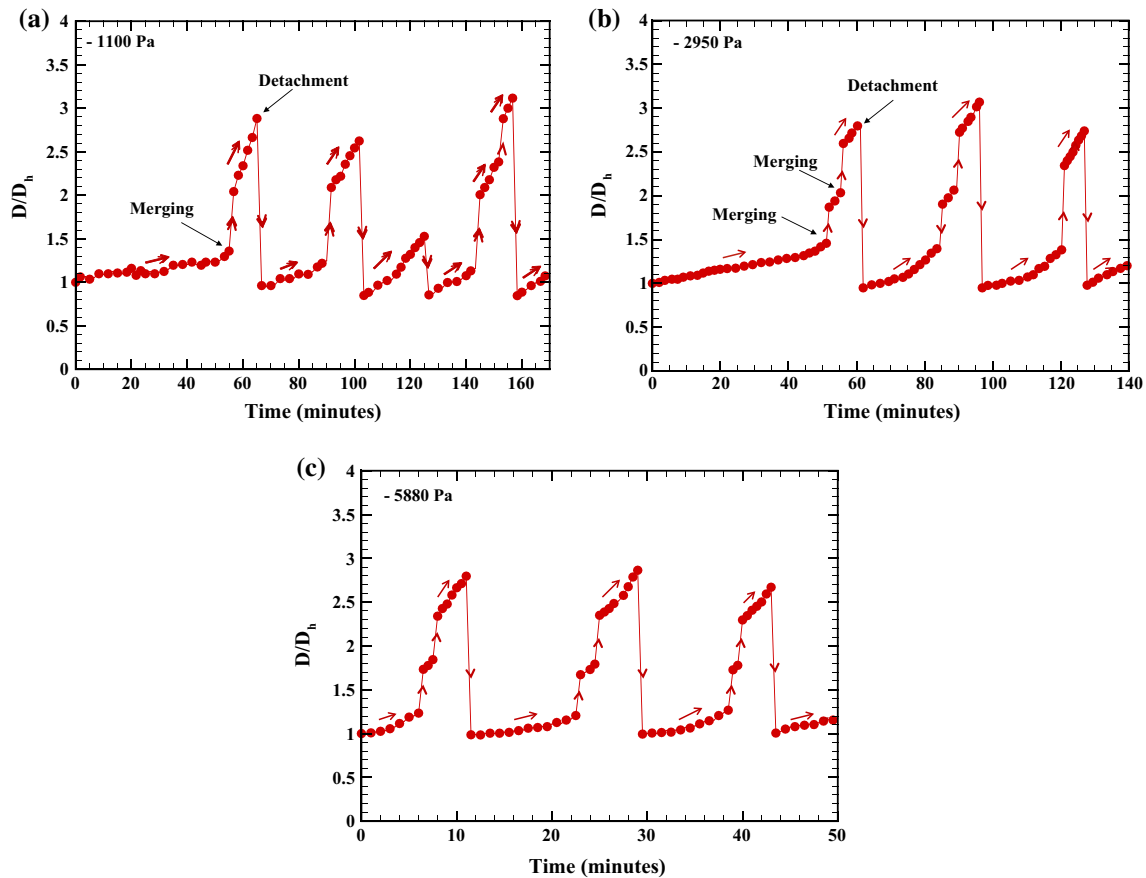
Fig. 5 Variation in the bubble size (D) with time at channel pressures ($P_{channel}$) below atmospheric pressure. The time series shown corresponds to channel pressures ($P_{channel}$) of **a** −1100 Pa, **b** −2950 Pa and **c** −5880 Pa; the negative sign indicating the pressures is below atmospheric pressure. The *bubbles* show gradual growth, sudden size increases due to merger and sudden size decreases due to detachment in each case. Data corresponding to about three repetitions of this cycle are shown in each case, with the time period corresponding to this cycle decreasing significantly as the absolute pressure in the channel is lowered. The flow rate through the channel was maintained at 5 ml/s for all the cases, and all data are normalized by the hole diameter (D_h)

The measured normalized detachment diameter (D_d/D_h) decreases rapidly with flow rate, as shown in Fig. 7a, due to the increased drag on the bubble. These data show the average detachment diameter obtained from analyzing a set of about 20 detachments, with the variation in the quantity being indicated by the error bars. The detachment diameter (D_d) is seen to be roughly flat at low flow rates and then decreases rapidly at higher flow rates, with D_d expected to slowly asymptote to D_h at very large flow rates. On the other hand, there appears to be no significant effect of absolute pressure on the detachment diameter, as shown in Fig. 7b.

The bubble detachment diameter (D_d) from surfaces has been well studied, for example, by Klausner et al. (1993) in the case of forced convection boiling. At sufficient flow rates parallel to the surface, the detachment is in principle determined from a simple horizontal force balance between the drag force on the bubble (F_d) and the component of the surface tension force (F_{sx}) that opposes the drag

force, with all the other forces acting on the bubble being relatively negligible. As observed from our experimental visualizations, this appears to be the case in most of our studies with the bubble detaching and moving horizontally along the flow direction. The bubble Reynolds numbers at detachment in our studies are in the range of 400–600, where the drag force, $F_d \approx 1.7(3\pi\mu U D_d)$ from the fit of Mei and Klausner (1992), where μ is the viscosity, and U is the relative flow speed. The surface tension force (F_{sx}) that opposes the drag force can be calculated and is given by $F_{sx} = \sigma D_o f(\alpha, \beta)$ (Klausner et al. 1993), where σ is the surface tension, D_o is the bubble diameter at the wall, and $f(\alpha, \beta)$ is a function of the advancing (α) and receding (β) contact angles, respectively. At higher flow rates, as shown in Fig. 6d, where bubble mergers are prevented, the bubble is essentially anchored at the hole edge, and so the bubble diameter (D_o) at the wall will be the hole diameter (D_h). Under these conditions, as the flow rate Q (and hence U) is increased, the drag force (F_d) is proportional to ($U D_d$),
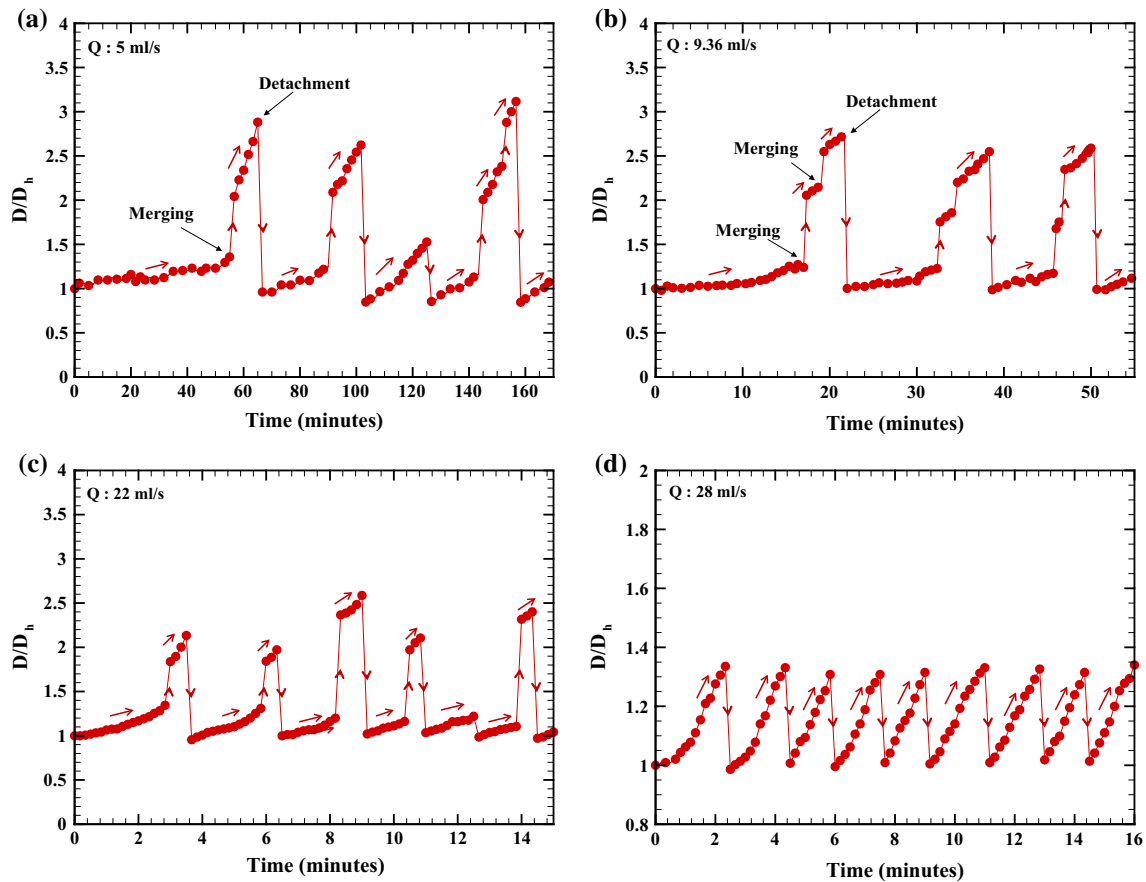
Fig. 6 Variation in the bubble size (D) with time for different flow rates through the channel, which shows a marked change in the time period of bubble growth and detachment with flow rate. The time series shown corresponds to **a** 5 ml/s, **b** 9.36 ml/s, **c** 22 ml/s and **d** 28 ml/s. The pressure inside the channel was maintained at 1100 Pa below the atmospheric pressure for all the cases, and all data are normalized by the hole diameter (D_h)
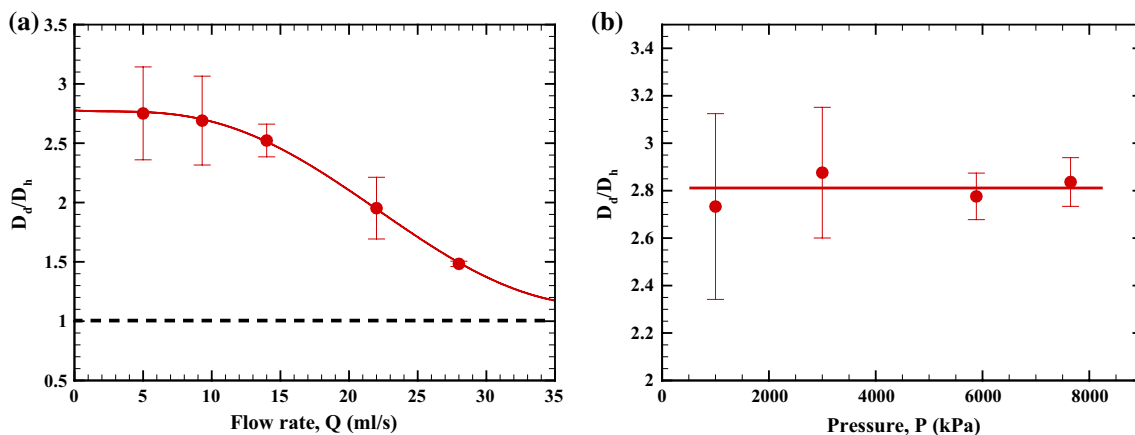

Fig. 7 Bubble detachment diameter as a function of **a** flow rate and **b** pressure inside the channel. The detachment diameter decreases with increasing discharge where it remains constant when pressure is varied

while the surface tension force (F_{sx}) is proportional to D_h, with all other factors in F_d and F_{sx} remaining fixed. Hence, the above simple analysis suggests that the detachment diameter (D_d) will vary inversely with the flow rate (or U) at higher flow rates, where bubble mergers are prevented. This is consistent with our observation in Fig. 7a. This simple
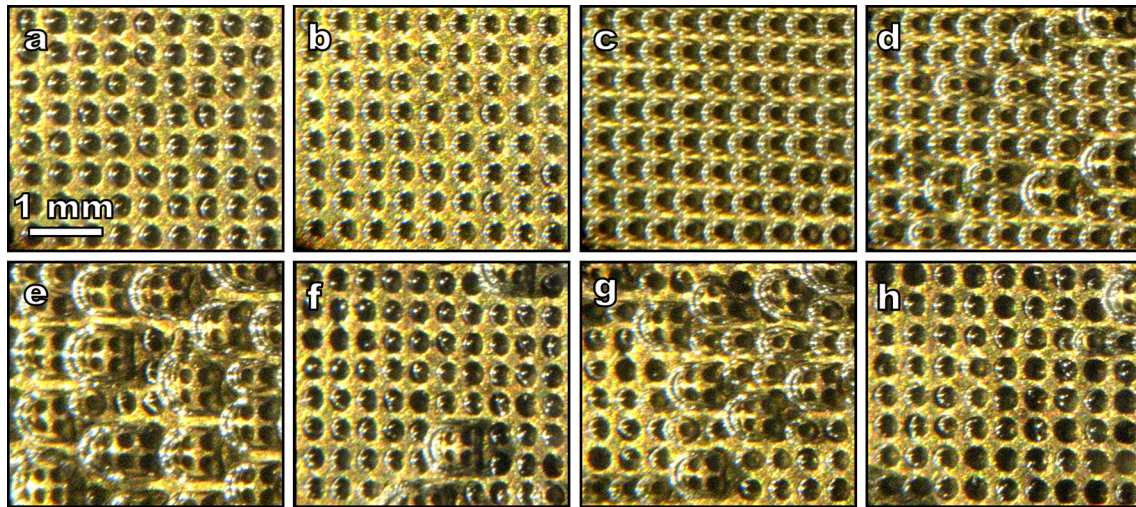
Fig. 8 Bubble distribution on the surface over a larger area at successive time instants for a pressure within the channel of 2950 Pa below atmospheric pressure and flow rate of 5 ml/s. The initial nearly uniform growth of the bubbles is followed at larger times by a more random state with bubbles growing, merging and detaching at various locations across the surface. Times after commencement of flow are **a** $t = 1$ min, **b** $t = 10$ min, **c** $t = 40$ min, **d** $t = 55$ min, **e** $t = 60$ min, **f** $t = 65$ min, **g** $t = 90$ min and **h** $t = 100$ min

analysis is, however, not valid at low flow rates, where the detachment diameter is large (about 2.75 D_h). In this case, the simple drag formula for a sphere in a uniform flow is no longer sufficient. Further, it is clear that as the flow rate decreases, the detachment criterion will at some point shift from a horizontal force balance to a vertical force balance between buoyancy and the vertical surface tension force, as discussed by Klausner et al. (1993). The change in the trend in the detachment diameter data at low flow rates, as shown in Fig. 7a, is probably caused by these effects.

Pressure drop resulting from the flow over the bubble mattress is an integral quantity and represents the combined effect of all the bubbles over the entire length of the textured surface and not just at a particular location. It should be noted that a single large bubble at any one point on the surface will increase the pressure drop. Hence, it is important to maintain bubble size uniformity over the entire surface. This is achieved by ensuring steady flow before changing the absolute pressure gradually to the required value within the channel. We show in Fig. 8a zoomed out picture of the air trapped on the textured surface over a large area at eight successive time instants. Figure 8a shows the initial condition when the bubbles have been trapped uniformly across the surface, with each hole containing an air bubble approximately of the same size. During the growth of the air bubbles (Fig. 8b, c), the change in the size of air bubbles is almost uniform across the entire surface. However, once the merging of bubbles begins (Fig. 8d), there is substantial variation across the surface. The merging process is random, with two bubbles merging at some locations and three or more bubbles merging at other

locations. Subsequent growth of the merged bubbles causes some of them to get detached from the surface, while the growth of other bubbles may still be happening at other locations (Fig. 8e). Further, in some cases when a big bubble detaches and gets carried away by the flow, it removes other bubbles on the same horizontal row where the first detachment occurred. After bubble detachment, nuclei of bubbles are left inside the holes (Fig. 8f), which in turn grow into large bubbles and the cycle of growth, merging and detachment continues (Fig. 8g).

The spatial variation in bubble size is illustrated in Fig. 9, which shows the normalized bubble diameter (D/D_h) plotted against time for several bubbles at different locations along the surface. Initially, the increase in diameter of the bubbles is seen to be uniform for different bubbles with all bubble data following nearly the same trend until around 40 min. Thereafter, merging begins and substantial variations can be seen between bubbles at different locations. At any given time instant, some bubbles are small ($\approx D_h$), while others can be substantially bigger due to merging ($\approx 3D_h$), and in general, there are bubbles at every stage of the bubble cycle that includes growth, merger and detachment. There is also the additional complication that when large merged bubbles detach from the surface and move into the flow, they may slide over the surface for a short distance and hence may carry other growing bubbles along with it. Hence, some of the growing bubbles get detached from the surface at much smaller diameters compared to the diameter to which it would have grown, if it was not carried away by other detaching large bubbles. After the initial 40 min, the pressure drop would then be related not
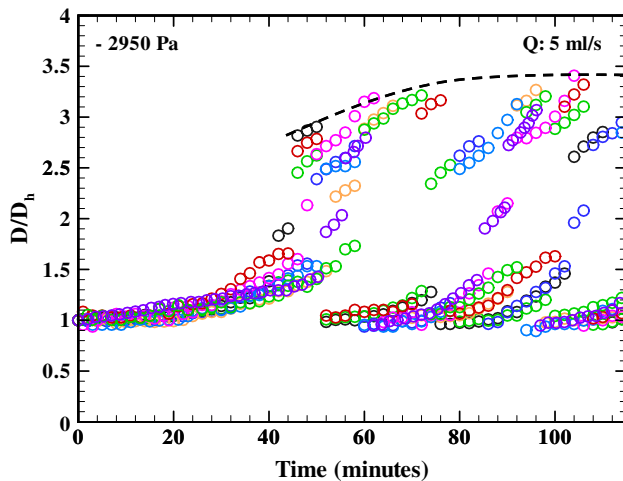
Fig. 9 Normalized bubble diameter (D/D_i) versus time for several bubbles at different locations along the surface in Fig. 8. The initial nearly uniform growth of the bubbles is followed at larger times by a more random state with bubbles growing, merging and detaching at various locations across the surface at any given time instant

Fig. 10 Measured pressure drop (ΔP) with time at a pressure inside the channel of 2950 Pa below the atmospheric pressure. The data shown here correspond to the bubble visualizations shown in Fig. 8, with the time instants corresponding to images (a–h) being also indicated here. The flow rate through the channel is 5 ml/s. The pressure drop increases as the bubble grows, and at all time instants are greater than the reference value

to any particular part of the bubble cycle, but to the spatially averaged bubble size over the entire surface, which would also be approximately the same as the time-averaged bubble size at any given location.

The time variation of pressure drop (ΔP) for a case corresponding to pressure within the channel ($P_{channel}$) that is lower than atmospheric pressure is shown in Fig. 10. The data correspond to the bubble visualization images shown in Fig. 8, with the time instants corresponding to the images (a–h) in Fig. 8 also marked on the pressure drop plot. Initially, when the bubbles grow uniformly over the surface [as in (a–c)], the pressure drop continually and gradually increases, reaching values that are more than twice the reference pressure drop, $\Delta P \approx 2 \, \Delta P_o$. Thereafter, the merging of air bubbles causes the pressure drop to increase further [as in (d) and (e)]. Following this [in images (f–h)], merged bubbles at a few sites are detaching from the surface, even as at other sites, growth and merging of the bubbles may still be taking place. This simultaneous growth, merging and detachment cause the pressure drop to undulate within a small range, which is apparent from pressure drop data between (f) and (h). It is clear that the growth of air bubbles causes an increase in pressure drop, with the ratio ($\Delta P/\Delta P_o$) always being greater than 1, and being about 2.5 with some variations at large times, corresponding to the highly unsteady bubble dynamics as seen in (f–h).

Variation of the pressure drop (ΔP) with time for different absolute pressures within the channel ($P_{channel}$) is shown in Fig. 11. As seen from the plots, the qualitative trends for the pressure drop variation with time are nearly the same in all cases. Initially, the pressure drop always increases
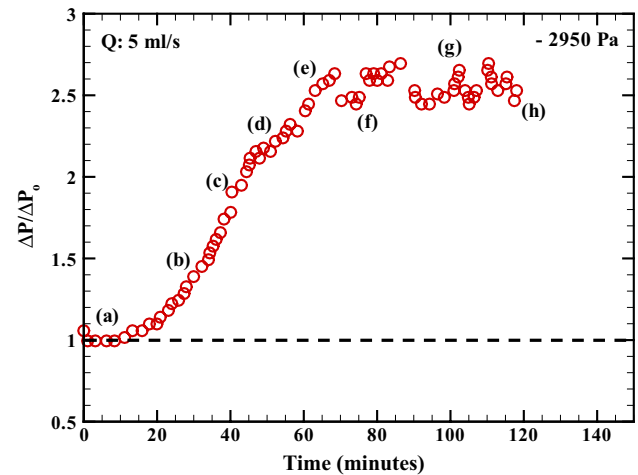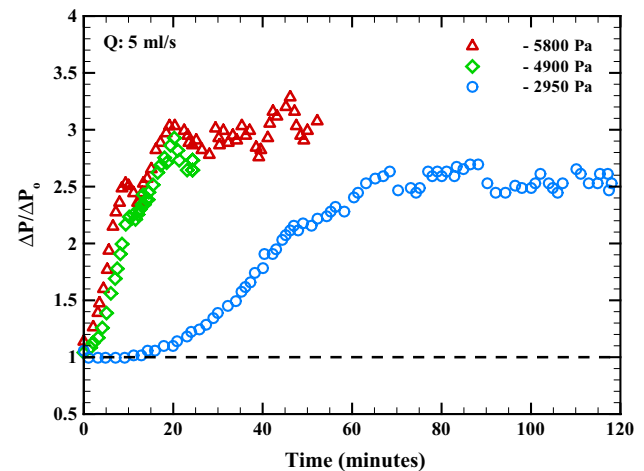

Fig. 11 Measured normalized pressure drop ($\Delta P/\Delta P_o$) with time corresponding to variations in absolute pressure within the channel. In all cases, the absolute pressure within the channel ($P_{channel}$) is lower than atmospheric pressure, as indicated by the negative values before pressure. The important difference caused by pressure variation is the rate of increase in pressure drop, which is consistent with the more rapid growth in the bubble size. The flow rate is kept constant at 5 ml/s

from values around the reference case and reaches large pressure drops that are a few times the reference value, corresponding to the state where the bubble dynamics has reached a quasi-steady state as shown in Fig. 8f–h. As seen before with the bubble dynamics, there is, however, a distinct change in the time scale as the absolute pressure
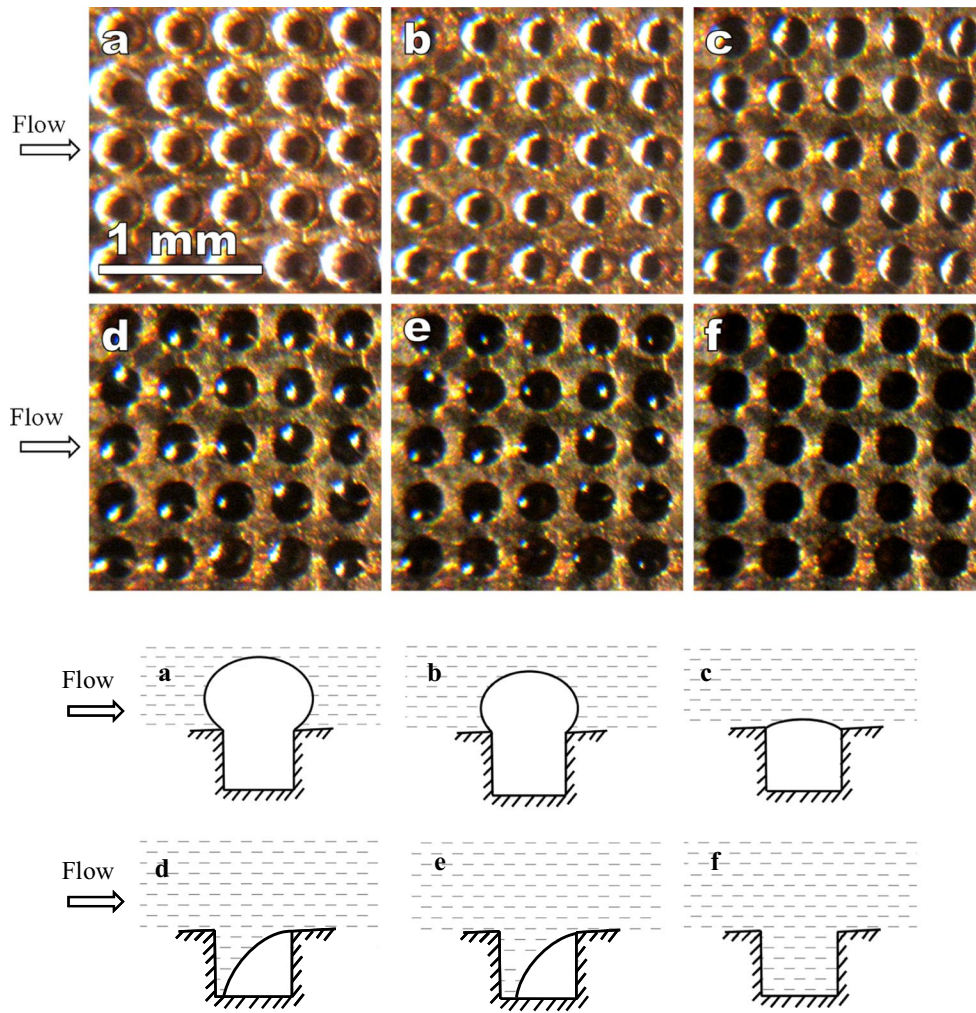
Fig. 12 Time sequence of images showing shrinkage of air bubbles when a pressure of 6850 Pa above atmospheric pressure is maintained inside the channel. The flow rate Q through the channel is 3.5 ml/s. The times after the flow commences are **a** $t = 0$ min, **b** $t = 5$ min, **c** $t = 40$ min, **d** $t = 75$ min, **e** $t = 115$ min and **f** $t = 150$ min. The bubbles shrink in size with time and eventually disappear. The schematics shown indicate the air–water interface corresponding to each of the time sequence of images

($P_{channel}$) is decreased, with the pressure drop (ΔP) increasing more rapidly at lower pressure, as shown in Fig. 11. Apart from this, one can also see that the value of pressure drop reached at large times does not vary significantly with pressure in Fig. 11, consistent with the fact that the detachment diameter shown in Fig. 7 does not vary significantly with pressure.

In summary, the pressure drop (ΔP) is found to be substantially larger than the reference case (ΔP_o), for all the cases where absolute pressure within the channel is lower than the atmospheric pressure ($P_{channel} < P_{atm}$). There is no drag reduction seen, and one in fact only observes large increase in pressure drop, of greater than 200 %, caused by the relatively large bubbles obstructing the flow.

4 Pressures within the channel above atmospheric pressure ($P_{channel} > P_{atm}$)

As the bubbles grow and obstruct the flow, the increased resistance to the flow is much higher than the reduction in the resistance due to low shear surface offered by the air surface. If the bubbles are allowed to shrink, then it should be possible to measure the reduced resistance through the pressure drop measurements. In this section, we study the flow characteristics when the pressure in the channel is maintained above atmospheric pressure ($P_{channel} > P_{atm}$). Figure 12 shows typical images of the trapped air pockets within the holes on the textured hydrophobic surface, recorded at regular time intervals, along with corresponding schematics of the air–water interface. The images

correspond to a pressure within the channel of 6850 Pa above atmospheric pressure, with a flow rate of 3.5 ml/s. Figure 12a shows the initial condition of the trapped air bubble, which is larger than the hole size, this being done to enable measurement of the pressure drop starting from large bubbles to near complete decay of the air bubble within the hole. The initial larger bubbles were achieved by maintaining a pressure lower than the atmospheric pressure (about 1100 Pa below atmospheric pressure) for a short period of time and controlling the duration of this pressure condition such that the bubbles do not merge with each other. After this short growth period, the pressure was made greater than atmospheric pressure. The shape of the air–water interface at this instant (Fig. 12a) indicates that the triple line is on the surface outside the hole. Subsequently, as seen in successive images from (a) to (f), the bubbles shrink in size and eventually are no longer visible by image (f) at time t of about 150 min. In the initial stages of bubble shrinkage, the diameter of the bubble just reduces, as in (a–c), as also depicted schematically in the bottom of the figure. At image (c), corresponding to about 40 min, the air bubbles have shrunk in size with the contact line pinned at the edges of the holes, and the bubbles appear to be almost flush with the holes. With time, the air bubbles shrink further into the hole and eventually get de-pinned from the edges (Fig. 12d). It was observed that the de-pinning occurs preferentially at the leading edge of the holes on the left, which is likely caused by the drag force on the bubble that pushes the bubble from left to right. At approximately 150 min, the air bubbles appear to have completely disappeared (Fig. 12f). This means either that all the air bubbles have completely disappeared or that they have become too small to be detected by the technique used to visualize the bubbles. The corresponding video showing bubble shrinkage is presented in Online Resource 2.

The pressure drop data are an integral quantity and represents the combined effect of all the trapped air over the entire length of the textured surface and not just at a particular location. Hence, we present in Fig. 13 a zoomed out picture of the air trapped on the textured surface over nearly its entire length at three successive time instants. This image was obtained using total internal reflection (TIR)-based imaging, as discussed in experimental methods section. With this technique, one can initially see bright spots in the image throughout the length of the surface, with each spot representing a trapped bubble within a hole, made visible by total internal reflection of light from the air–water interface. With time, the number of bright spots on the surface diminishes, and at a time of about 60 min, the number of spots has greatly reduced. However, it may be noted that the distribution at any given streamwise location is roughly similar, indicating that the bubble behavior shown in Fig. 12 at a few holes is reasonably representative
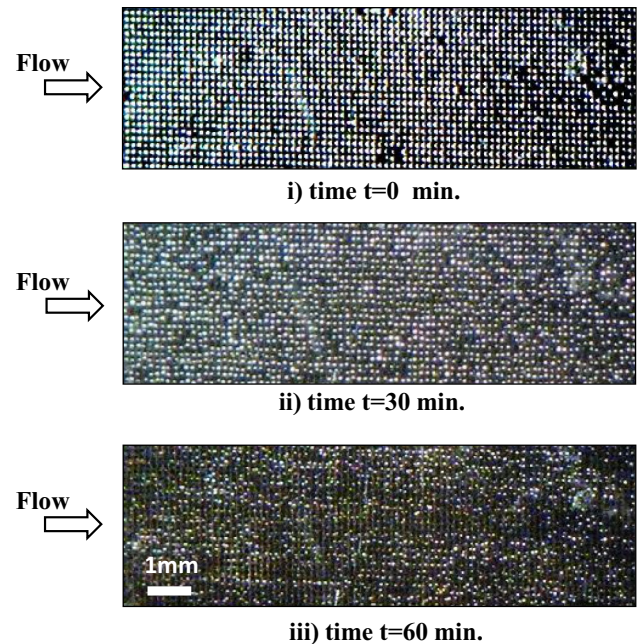
Fig. 13 Time sequence of disappearance of air bubbles at a pressure of 6850 Pa above the atmospheric pressure inside the channel. The flow rate through the channel is 6.5 ml/s. Initially, the air bubbles cover the entire surface. With time, the air bubbles shrink in size and eventually disappear
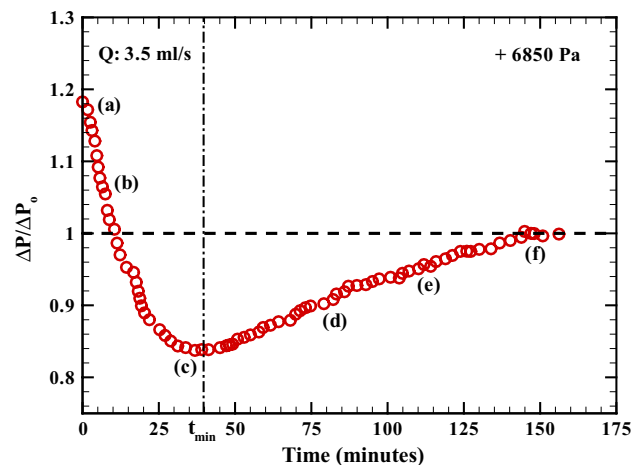

Fig. 14 Measured pressure drop (ΔP) with time at a pressure inside the channel of 6850 Pa above the atmospheric pressure. The data shown here correspond to the bubble visualizations shown in Fig. 12, with the time instants corresponding to images (a–f) being also indicated here. The flow rate through the channel is 3.5 ml/s. The pressure drop data reduce from greater than the reference value, as the bubble shrinks, reaching a minimum corresponding to about 15 % pressure drop reduction when the bubble is flush with the hole, and then slowly increasing to the reference pressure drop value

of the entire textured surface. The measured pressure drop would thus be expected to respond to this observed decay of air bubbles over the entire length of the textured surface.

The pressure drop data corresponding to the bubble dynamics presented in Fig. 12 are shown in Fig. 14. The pressure drop (ΔP) data in the plot have been normalized by the pressure drop through the channel at the same flow rate (3.5 ml/s) from the reference case (ΔP_o) in Fig. 3, with the time instants corresponding to the images (a–f) in Fig. 12 also marked on the plot. Initially, when the bubble size is large [as in (a)], the pressure drop obtained is much higher than that obtained at the same flow rate for the reference pressure drop shown by the dashed line (ΔP_o). As the bubbles begin to shrink in size (as in (b)), there is a corresponding decrease in pressure drop. With further decrease in bubble size, the pressure drop decreases below the reference value and reaches a minimum corresponding to about $0.85\Delta P_o$ that represents a pressure drop reduction (or drag reduction) of about 15 % corresponding to the instant (c). At this instant, the bubble as indicated in Fig. 12 is nearly flush with the hole, and this appears to be the optimal condition for maximum reduction in pressure drop. Subsequently, the pressure drop increases and finally reaches that of the reference pressure drop, as the bubble slowly recedes into the hole [as in (d) and (e)] and finally is no longer visible [as in (f)]. The maximum drag reduction is about 15 % and occurs at a time of about 40 min, which we shall refer to as t_{min}.

The pressure drop data (ΔP) normalized by the reference pressure drop (ΔP_o) and plotted versus ($t - t_{min}$) are shown in Fig. 15a for absolute pressure variation and in Fig. 15b for flow rate variation. As seen from the plots, the qualitative trends for the pressure drop variation with time are the same in all cases. The measured pressure difference (ΔP) decreases initially from values greater than the reference case (ΔP_o), reaching a minimum (at t_{min}) that is lower than the reference value, and then gradually increases to the reference value given sufficient time. The important difference caused by pressure variation in (a) and flow rate variation in (b) is the time scale. For example, the time taken to go from the minimum pressure drop condition to the reference value substantially increases as the pressure or flow rate is decreased. This implies that the duration of time for which drag reduction can be sustained can be increased by decreasing the absolute pressure within the channel.

5 Discussion

The visualization of entrapped air bubbles revealed that when the absolute pressure in the channel is maintained below the atmospheric pressure ($P_{channel} < P_{atm}$), the size of the air bubbles gradually increased, resulting in merger of adjacent bubbles, followed by bubble detachment from the surface. On the contrary, when the pressure is maintained above the atmospheric pressure ($P_{channel} > P_{atm}$) there is a
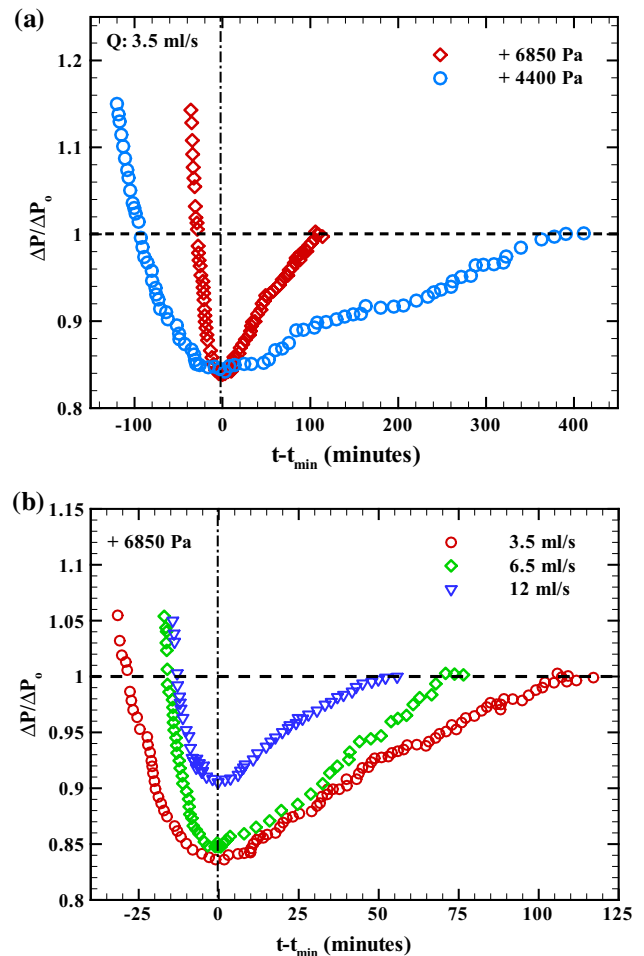

Fig. 15 Measured normalized pressure drop ($\Delta P/\Delta P_o$) with time corresponding to variations in **a** absolute pressure within the channel and **b** flow rate. The important difference caused by pressure variation in (a) and flow rate variation in (b) is the time taken to go from the minimum pressure drop condition to the reference value (ΔP_o), which substantially decreases as the pressure or flow rate is increased. In (**a**), flow rate is kept constant at 3.5 ml/s, while in (**b**), the pressure within the channel is maintained close to (+) 6850 Pa above atmospheric pressure in all cases

gradual decrease in size of air bubbles with time, leading to their eventual disappearance. This indicates that changes in the absolute pressure of water close to the surface can substantially alter the trapped air bubble dynamics, which in turn affect the pressure drop (ΔP) through the channel.

From Henry's law, it can be shown that any variation of pressure within the channel would result in a change in the degree of saturation (f) of air in water within the channel. In our experiments, water was saturated at room temperature and atmospheric pressure (P_{atm}) and was exposed to a different pressure inside the channel ($P_{channel}$), which was either greater or lesser than P_{atm}. The degree of saturation of water within the channel under these conditions is given by:

$$f = \frac{P_{\text{atm}}}{P_{\text{channel}}}$$

Hence, in the case of absolute pressures within the channel that are lower than atmospheric pressure ($P_{\text{channel}} < P_{\text{atm}}$), the degree of saturation f would be greater than 1, implying that the water will be supersaturated with air, leading to transport of air from the water into the trapped air bubbles. On the contrary, at pressures above atmospheric pressure ($P_{\text{channel}} > P_{\text{atm}}$), f would be lesser than 1, implying that the water will be undersaturated with air, leading to transport of air from the trapped air bubbles to the water.

The rate of growth or dissolution of a stationary spherical bubble suspended in a stationary infinite medium (water) with air concentration (C_∞) is given by the Epstein–Plesset equation (Epstein and Plesset 1950) as:

$$\left(\frac{D}{D_i}\right)^2 = 1 - \left[\frac{8kC_s(1-f)}{\rho D_i^2}\right]t$$

where D is the diameter of the bubble at time t, D_i is the initial diameter, k is the diffusivity of air in water, ρ is the density of air, f is the degree of saturation ($f = C_\infty/C_s$), C_s being the saturation concentration of air in water.

In flow situations, rate of growth or dissolution of the bubbles is more pronounced due to convective effects caused by the flow. In this case, the rate of mass transfer of air from or to the bubble is given by:

$$\dot{m}_a = h_m A_s (C_s - C_\infty)$$

where h_m is the convective mass transfer coefficient, A_s is the surface area of the air bubble, and ($C_s - C_\infty$) is the difference in the concentration of air in water at the surface of the bubble and at a location far away from it. This mass transfer coefficient when expressed in a dimensionless form is called the Sherwood number and is given as:

$$Sh = \frac{h_m D}{k}$$

where D is the diameter of the bubble and k is the diffusivity. For a spherical bubble exposed to flow, Favelukis et al. (1995) have showed that Sherwood number scales with the Peclet number ($Pe = UD/k$, U being the flow velocity relative to the bubble) as:

$$Sh \sim Pe^{1/2}$$

with this scaling being valid for $Pe \gg 1$, where convection is much stronger than diffusion, as in the present case. This convective mass transfer leads to a change in the diameter of the bubble (D) with time from its initial value (D_i), which, from Eqs. (2)–(4), can be shown to be of the functional form:

$$\left(\frac{D}{D_i}\right)^{3/2} = 1 + st$$

where s is a parameter which depends on the degree of saturation f and is given by:

$$s = a\frac{3C_s}{\rho}(f-1)(kU)^{1/2}D_i^{-3/2},$$

where a is a proportionality constant from Eq. (4). This functional form for the variation of D is consistent with the expression for a growing bubble in a flow obtained by Al-Hayes and Winterton (1981) and may be contrasted with Eq. (1) for the case with no flow, where the exponent for D is 2 as compared to the present case where it is (3/2). Further, the expression [Eq. (6)] clearly shows that the diameter (D) of the bubble grows if $f > 1$ and decays for $f < 1$, with the magnitude of the growth/decay being dependent both on the magnitude of ($f-1$) and the relative flow velocity U between the bubble and the flow, the latter being dependent on Q.

The measured growth/decay of the trapped air bubbles with time in our experiments can be compared with the (D/D_i)$^{3/2}$ variation. With this in mind, we show in Fig. 16 our measured bubble diameter (D) plotted in the form of (D/D_i)$^{3/2}$ with time. The data corresponding to $P_{\text{channel}} < P_{\text{atm}}$, where the bubble grows with time, are shown in Fig. 16a, and the data for $P_{\text{channel}} > P_{\text{atm}}$, where the bubbles decay, are shown in Fig. 16b. As seen in the plots, the variation in the data is nearly linear for all time in (a). In the case of (b), the data are again linear at small times. At later times, when (D/D_i) < 0.8 (or (D/D_i)$^{3/2}$ < 0.7), the slope appears to reduce. This is due to the fact that the air–water interface has shrunk into the hole, as shown in Fig. 12d, and as a result the removal of air occurs at a lesser rate.

In both cases in (a) and (b), the slope of the data at small times gives the parameter s in Eq. 5. The variation in s corresponding to 16a, b is shown in Fig. 16c, d, respectively. The growth rate in (c) increases linearly with f for $f > 1$, while for $f < 1$ in (d), the decay rate in (d) increases linearly as f is decreased from 1.0. In the case of $P_{\text{channel}} < P_{\text{atm}}$ ($f > 1$), as the pressure is lowered, the growth rate increases significantly, this growth rate corresponding to the initial phase of growth of a single bubble before merger. In the case of $P_{\text{channel}} > P_{\text{atm}}$ ($f < 1$), this leads to a more rapid decay in size of the trapped air pockets or bubbles as the pressure is increased consistent broadly with earlier results (Poetes et al. 2010; Samaha et al. 2012b, d; Dilip et al. 2014).

Apart from the degree of saturation f, the rate of growth/decay of the bubble is also affected by the flow rate of water Q through the channel. The data corresponding to supersaturated water with a degree of saturation of $f = 1.05$, where the bubble grows with time, are shown in Fig. 17a, and the data
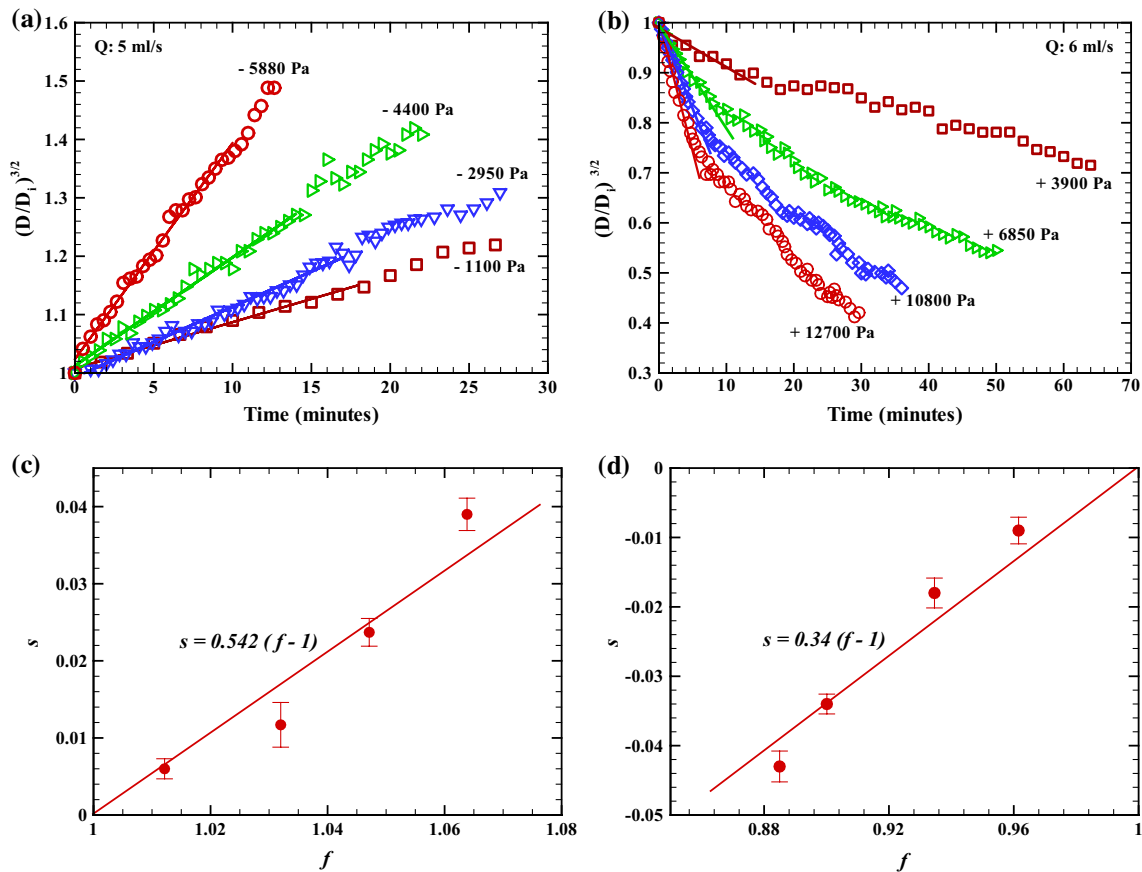
Fig. 16 Bubble growth/decay with time at different degree of saturation (f) of water within the channel. In (**a**), growth of bubbles is shown for different values of degree of saturation f, when water is supersaturated with air ($f > 1$), while in (**b**), decay of bubbles at vari-

ous f when water is undersaturated ($f < 1$) is shown. Variation in the initial slopes of the data (s) in (**a**) and (**b**) is shown in (**c**) and (**d**), respectively

for undersaturated water at degree of saturation $f = 0.93$, where the bubbles decay, are shown in Fig. 17b. In the former case, a higher flow rate causes the bubbles to grow more rapidly, whereas in the latter case, an increase in the flow rate causes the bubbles to shrink faster, consistent with Eqs. (5) and (6). From the data in Fig. 17a, b, the parameter s in Eq. 5 may be found as the slope of the data at small times. The variation in s corresponding to 17a, b is plotted against the flow rate Q and is shown in Fig. 17c, d, respectively. The slope s is expected to vary as $U^{0.5}$ from Eq. (6), and the actual variation shown in Fig. 17c, d is found to be broadly consistent with this, as shown by the $Q^{0.5}$ fits in both cases; s increasing for $f > 1$ and decreasing for $f < 1$.

Pressure drop (ΔP) measurements indicate that the growth of air bubbles at absolute pressures within the channel that are lower than atmospheric values ($P_{channel} < P_{atm}$) causes the pressure drop to increase above the reference value (ΔP_o) corresponding to the Wenzel state, i.e., when the holes are completely filled with water. This is illustrated in Fig. 18a, where the pressure drop data are plotted against the bubble

diameter D normalized with the diameter of the hole D_h for such a case. As the bubbles grow, the pressure drop substantially increases, and at later times, once bubble merging and detachment have begun, the pressure drop continues to be significantly large, about 250 % of the reference case. This is due to the fact that the growing air bubbles obstruct the flow passage, with the whole flow field also being highly unsteady, and this manifests as an increase in the pressure drop. At later times corresponding to the large nearly saturated pressure drop, bubble growth, merger and detachment occur at each instant in different parts of the surface, as depicted by the schematics in Fig. 18a. It is thus clear that merely having bubbles is not sufficient, it can in fact be much worse in terms of pressure drop than even the reference Wenzel condition.

On the other hand, when the pressure in the channel was maintained greater than atmospheric pressure ($P_{channel} > P_{atm}$), the pressure drop decreased to a minimum value, which was lower than the reference Wenzel case, and then gradually increased to become equal to the reference pressure drop. This is illustrated by a typical pressure drop
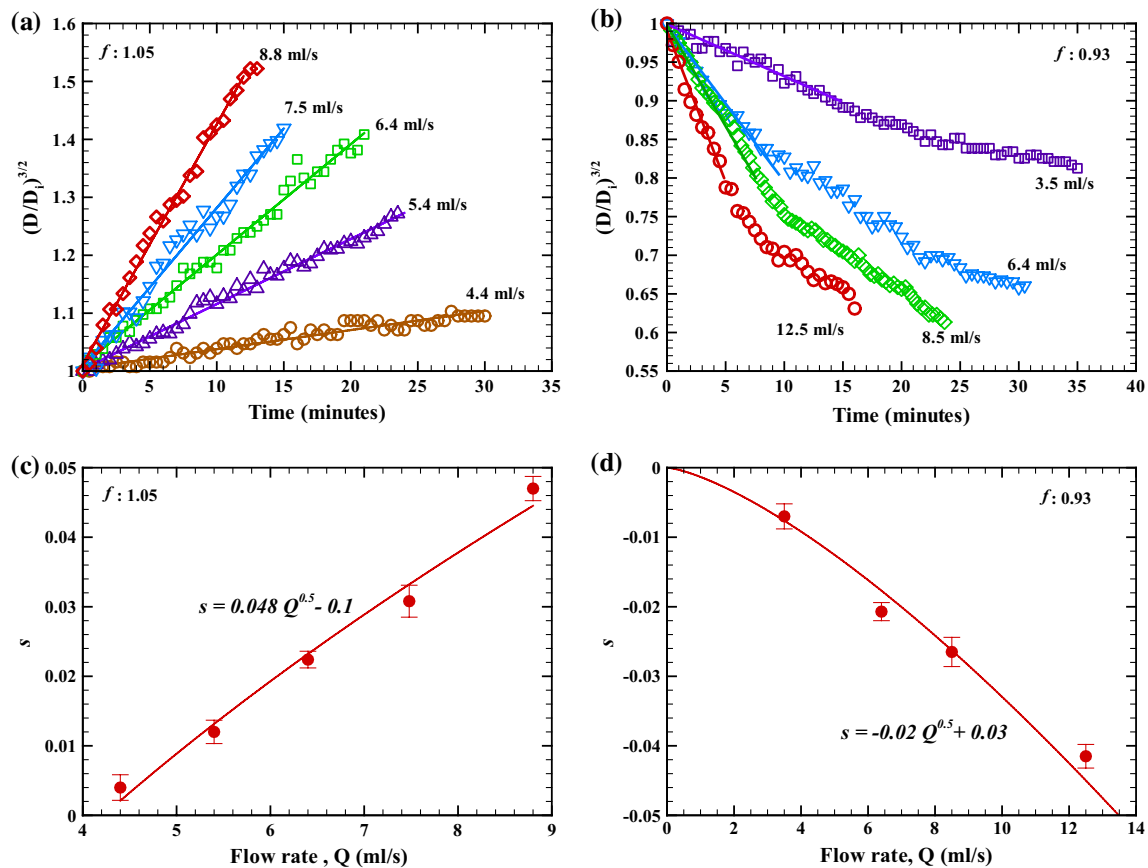
Fig. 17 Bubble growth/decay with time at various flow rates of water through the channel. In (**a**), growth of bubbles is shown for different values Q, when water is supersaturated with air ($f = 1.05$), while in (**b**), decay of bubbles at various Q when water is undersaturated ($f = 0.93$) are shown. Variation in the initial slopes of the data (s) in (**a**) and (**b**), plotted against the flow rate, is shown in (**c**) and (**d**), respectively

versus normalized bubble diameter curve for such a case in Fig. 18b with schematics showing the water–air interface at a few time instants. As the bubbles initially shrink in size, the pressure drop also reduces with time. The minimum pressure drop is found to correspond to the instant when the bubbles are flush with the surface, i.e., near $D/D_h = 1$ as shown in the figure. This observation is in agreement with the recent analytical and numerical studies of Steinberger et al. (2007), Havuyoloma and Harting (2008), Davis and Lauga (2009), and Wang et al. (2014) who found that the maximum slip length occurs at an optimum bubble shape, and any variation from this optimum condition would cause the slip length to reduce. We show in this work that the absolute pressure within the channel ($P_{channel}$) significantly changes the time scale over which the pressure drop reduction is observed, with the time scale increasing as the pressure within the channel approaches the atmospheric pressure, where the water is saturated with air. The present work has been done for a particular textured surface, namely a surface with holes. However, the broad result of changes in $P_{channel}$ significantly affecting the time scale over which the pressure drop reduction is observed is expected to occur for all patterned surfaces, although the precise dependence of drag on absolute channel pressure would be texture-dependent. This result can be useful in sustaining drag reduction over large periods of time in internal flows such as those in microchannels.

6 Conclusions

We present results on the flow past an array of air bubbles formed over a textured hydrophobic surface containing a regular array of blind holes. The surface was generated using photo-etching of brass and rendered hydrophobic through a self-assembled monolayer coating. The diameter of the holes was 300 μm, pitch 370 μm and depth 160 μm, with the contact angle measured on the surface being 125°. This surface is used as one wall of a microchannel, and the flow through this microchannel is studied for varying absolute pressures within the channel ($P_{channel}$). We visualize in all cases the trapped air bubbles on the textured surface
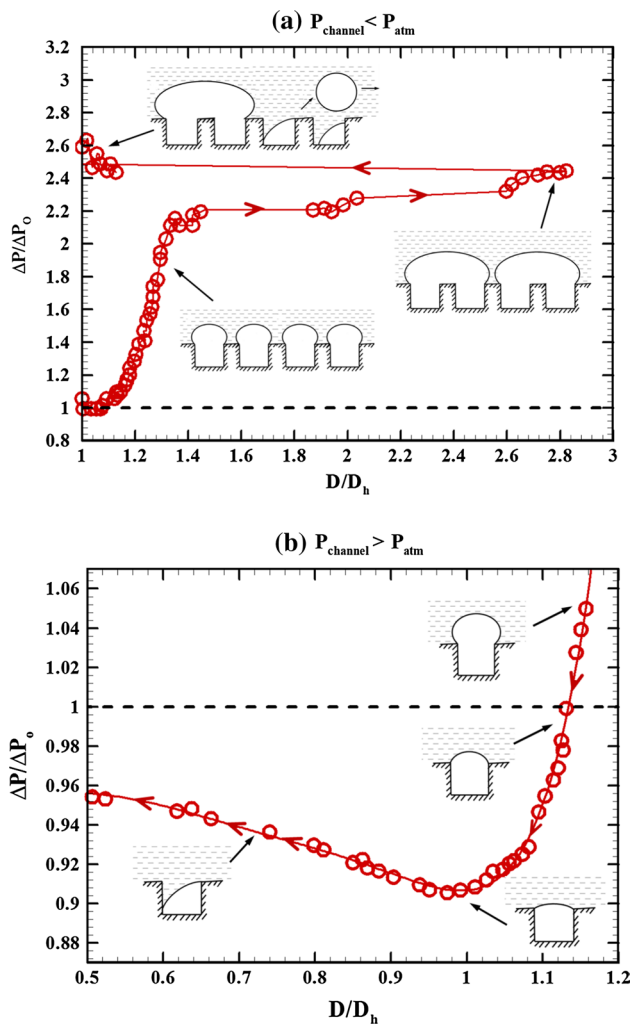
Fig. 18 Pressure drop versus normalized bubble diameter in flow through a textured hydrophobic microchannel with schematics showing the corresponding water–air interface. In (**a**), the absolute pressure within the channel is lower than the atmospheric pressure ($P_{channel} < P_{atm}$), and hence, the water within the channel is supersaturated with air. In (**b**), the absolute pressure within the channel is higher than the atmospheric pressure ($P_{channel} > P_{atm}$), and hence, the water within the channel is undersaturated with air. The pressure drop data in the two cases are entirely different, with (**a**) having large pressure drop increase, while (**b**) has a pressure drop reduction over a period of time

with simultaneous measurements of the pressure drop (ΔP) through the channel, both as a function of time.

When the absolute pressure within the channel is lower than atmospheric pressure ($P_{channel} < P_{atm}$), we find that the trapped air bubbles grow with time, merge with adjacent bubbles and then detach from the surface. This whole process is driven by the fact that the water in the channel is effectively supersaturated with air, and hence, air gets transported from the water into the trapped air bubbles on the surface. We show that as the pressure is lowered from atmospheric pressure, the trapped air

bubbles grow more rapidly with time, and the bubble cycle time for growth, merger and detachment decreases. The flow rate is also found to have a significant effect both on the time scale for bubble growth and on the maximum bubble diameter reached before the bubble detaches from the surface. Simultaneous pressure drop measurements show that in these cases, there is a large increase in pressure drop compared to the reference case with no air trapped on the textured surface. Hence, it is clear that the mere presence of air is not sufficient to give drag reduction. We in fact get large, up to about 250 %, increase in pressure drop compared to the reference value in these cases.

On the other hand, when the absolute pressure within the channel is larger than the atmospheric pressure ($P_{channel} > P_{atm}$), we find that the trapped air bubbles decay with time, as reported by others. This process is driven by the fact that the water in the channel is in this case undersaturated with air, and hence, air transport occurs from the trapped air bubbles into the water in the channel. The decay or shrinking of the trapped air bubbles initially occurs outside the holes, with the air–water interface then slowly moving into the holes on the surface. Simultaneous pressure drop (ΔP) measurements show that in these cases there can be a substantial decrease in pressure drop that is achieved for a certain period of time. Actual pressure drop versus time curves indicate a period for which this drag reduction is observed, this time being dependent on the absolute pressure within the channel ($P_{channel}$). The maximum pressure drop reduction, of about 15 %, is achieved at an intermediate time corresponding to the instant when the trapped air bubble is flush with the surface. At times before this, the bubbles are larger and protrude into the flow, while at later times, the air–water interface enters the hole, with the pressure drop being larger than the instant when the trapped air bubble is flush with the surface. At very large times, the air–water interface goes deep within the hole and the pressure drop asymptotes to the reference value in the absence of any air.

In summary, we show in the present work that the absolute pressure within a textured hydrophobic channel can significantly alter the dynamics of the trapped air bubbles on the surface, which can have a profound effect on the pressure drop through the channel. At low channel pressures, the trapped air bubbles grow, merge and detach from the surface, with this resulting in a large pressure drop increase, despite the presence of air. On the other hand, at higher pressures, pressure drop reduction is achieved, with the maximum pressure drop occurring when the bubble is flush with the surface, although the time scale for which this occurs is dependent on the absolute pressure within the channel.

References

Al-Hayes RAM, Winterton RHS (1981) Bubble growth in flowing liquids. Int J Heat Mass Transf 24:213–221

Bixler GD, Theiss A, Bhushan B, Lee SC (2014) Anti-fouling properties of microstructured surfaces bio-inspired by rice leaves and butterfly wings. J Colloid Interface Sci 419:114–133

Bobji MS, Kumar SV, Asthana A, Govardhan RN (2009) Underwater sustainability of the "Cassie" state of wetting. Langmuir 25:12120–12126

Bobji MS, Balan G, Govardhan RN (2011) Time dependant hydrophobicity of drag reducing surfaces. In: 3rd Micro and nano flows conference, Thessaloniki, Greece, 22–24 August 2011

Bormashenko E (2015) Progress in understanding wetting transitions on rough surfaces. Adv Colloid Interface Sci 222:92–103

Celia E, Darmanin T, Taffin de Givenchy E, Amigoni S, Guittard F (2013) Recent advances in designing superhydrophobic surfaces. J Colloid Interface Sci 402:1–18

Checco A, Ocko BM, Rahman A, Black CT, Tasinkevych M, Giacomello A, Dietrich S (2014) Collapse and reversibility of the superhydrophobic state on nanotextured surfaces. Phys Rev Lett 112:216101

Cheng Y-T, Rodak DE (2005) Is the lotus leaf superhydrophobic? Appl Phys Lett 86:144101

Choi CH, Westin KJA, Breuer KS (2003) Apparent slip flows in hydrophilic and hydrophobic microchannels. Phys Fluids 15:2897–2902

Choi CH, Ulmanella U, Kim J, Ho CM, Kim CJ (2006) Effective slip and friction reduction in nanograted superhydrophobic microchannels. Phys Fluids 18:087105

Cong Q, Chen G, Fang Y, Ren L (2004) Super-hydrophobic characteristics of butterfly wing surface. J Bionics Eng 1:249–255

Davis AMJ, Lauga E (2009) Geometric transition in friction for flow over a bubble mattress. Phys Fluids 21:011701

Dilip D, Jha NK, Govardhan RN, Bobji MS (2014) Controlling air solubility to maintain "Cassie" state for sustained drag reduction. Colloids Surf A Physicochem Eng Asp 459:217–224

Emami B, Hemeda AA, Amrei MM, Luzar A, Gad-el-Hak M, Tafreshi HV (2013) Predicting longevity of submerged superhydrophobic surfaces: surfaces with parallel grooves. Phys Fluids 25:062108

Epsein PS, Plesset MS (1950) On the stability of gas bubbles in liquid-gas solutions. J Chem Phys 18:1505–1509

Favelukis M, Tadmor Z, Talmon Y (1995) Bubble dissolution in viscous liquids in simple shear flow. AIChE J 41:2637–2641

Flynn MR, Bush JWM (2008) Underwater breathing: the mechanics of plastron respiration. J Fluid Mech 608:275–296

Gao X, Jiang L (2004) Water-repellent legs of water striders. Nature (London) 432:36

Gogte S, Vorobieff P, Truesdell R, Mammoli A, van Swol F, Shah P, Brinker CJ (2005) Effective slip on textured superhydrophobic surfaces. Phys Fluids 17:051701

Govardhan RN, Srinivas GS, Asthana A, Bobji MS (2009) Time dependence of effective slip on textured hydrophobic surfaces. Phys Fluids 21:052001

Hemeda AA, Tafreshi HV (2014) General formulations for predicting longevity of submerged superhydrophobic surfaces composed of pores or posts. Langmuir 30:10317–10327

Hemeda AA, Gad-el-Hak M, Tafreshi HV (2014) Effects of hierarchical features on longevity of submerged superhydrophobic surfaces with parallel grooves. Phys Fluids 26:082103

Hensel R, Finn A, Helbig R, Killge S, Braun HG, Werner C (2014) In situ experiments to reveal the role of surface feature sidewalls in the Cassie − Wenzel transition. Langmuir 30:15162–15170

Hu DL, Chan B, Bush JWM (2003) The hydrodynamics of water strider locomotion. Nature (London) 424:663

Hyvaluoma J, Harting J (2008) Slip flow over structured surfaces with entrapped microbubbles. Phys Rev Lett 100:246001

Klausner JF, Mei R, Bernhard DM, Zeng LZ (1993) Vapor bubble departure in forced convection boiling. Int J Hcat Mass Transf 36:651–662

Koch K, Barthlott W (2009) Superhydrophobic and superhydrophilic plant surfaces: an inspiration for biomimetic materials. Phil Trans R Soc A 367:1487–1509

Larmour IA, Bell SEJ, Saunders GC (2007) Remarkably simple fabrication of superhydrophobic surfaces using electroless galvanic deposition. Angew Chem Int Ed 46:1710–1712

Lauga E, Stone H (2003) Effective slip in pressure-driven stokes flow. J Fluid Mech 489:55–77

Lee C, Choi C-H, Kim CJ (2008) Structured surfaces for a giant liquid slip. Phys Rev Lett 101:064501

Liebermann L (1957) Air bubbles in water. J Appl Phys 28:205–211

Lv P, Xue Y, Shi Y, Lin H, Duan H (2014) Metastable states and wetting transition of submerged superhydrophobic structures. Phys Rev Lett 112:196101

Lv P, Xue Y, Liu H, Shi Y, Xi P, Lin H, Duan H (2015) Symmetric and asymmetric meniscus collapse in wetting transition on submerged structured surfaces. Langmuir 31:1248–1254

Mei R, Klausner JF (1992) Unsteady force on a spherical bubble at finite Reynolds number with small fluctuations in the free-stream velocity. Phys Fluids 4:63–70

Ou J, Rothstein JP (2005) Direct measurements on flow past drag-reducing ultrahydrophobic surfaces. Phys Fluids 17:103606

Ou J, Perot B, Rothstein JP (2004) Laminar drag reduction in microchannels using ultrahydrophobic surfaces. Phys Fluids 16:4635–4643

Pan Q, Wang M, Wang H (2008) Separating small amount of water and hydrophobic solvents by novel superhydrophobic meshes. Appl Surf Sci 254:6002–6006

Parker AR, Lawrence CR (2001) Water capture by a desert beetle. Nature (London) 414:33

Piao L, Park H (2015) Two-dimensional analysis of air-water interface on superhydrophobic grooves under fluctuating water pressure. Langmuir 31:8022–8032

Poetes R, Holtzmann K, Franze K, Steiner U (2010) Metastable Underwater Superhydrophobicity. Phys Rev Lett 105:166104

Rothstein P (2010) Slip on Superhydrophobic surfaces. Annu Rev Fluid Mech 42:89–109

Samaha MA, Tafreshi HV, Gad-el-Hak M (2012a) Effects of hydrostatic pressure on the drag reduction of submerged aerogel-particle coatings. Colloids Surf A Physicochem Eng Asp 399:62–70

Samaha MA, Tafreshi HV, Gad-el-Hak M (2012b) Influence of Flow on longevity of superhydrophobic coatings. Langmuir 28:9759–9766

Samaha MA, Tafreshi HV, Gad-el-Hak M (2012c) Superhydrophobic surfaces: from the lotus leaf to the submarine. C R Mec 340:18–34

Samaha MA, Tafreshi HV, Gad-el-Hak M (2012d) Sustainability of Superhydrophobicity under pressure. Phys Fluids 24:112103

Sheng X, Zhang J (2011) Air layer on superhydrophobic surfaces under water. Colloids Surf A Physiochem Eng Asp 377:374–378

Shirtcliffe NJ, McHale G, Newton MI, Perry CC, Pyatt FB (2006) Plastron properties of a superhydrophobic surface. Appl Phys Lett 89:104106

Shirtcliffe NJ, McHale G, Atherton S, Newton MI (2010) An introduction to superhydrophobicity. Adv Colloid Interface Sci 161:124–138

Søgaard E, Andersen NK, Smistrup K, Larsen ST, Sun L, Taboryski R (2014) Study of transitions between wetting states on microcavity arrays by optical transmission microscopy. Langmuir 30:12960–12968

Steinberger A, Cottin-Bizonne C, Kleimann P, Charlaix E (2007) High friction on a bubble mattress. Nat Mater 6:665–668

Teo CJ, Khoo BC (2009) Analysis of Stokes flow in microchannels with superhydrophobic surfaces containing a periodic array of micro-grooves. Microfluid Nanofluid 7:353–382

Tretheway C, Meinhart CD (2002) Apparent fluid slip at hydrophobic microchannel walls. Phys Fluids 14:L9–L12

Truesdell R, Mammoli A, Vorobieff P, van Swol F, Jeffrey Brinker C (2006) Drag reduction on a patterned superhydrophobic surface. Phys Rev Lett 97:044504

Verho T, Korhonen JT, Sainiemi L, Jokinen V, Bower C, Franze K, Franssila S, Andrew P, Ikkala O, Ras RH (2012) Reversible switching between superhydrophobic states on a hierarchically structured surface. Proc Natl Acad Sci 109:10210–10213

Wang LP, Teo CJ, Khoo BC (2014) Effect of Interface deformation on flow through microtubes containing superhydrophobic surfaces with longitudinal ribs and grooves. Microfluid Nanofluid 16:225–236

Watanabe K, Udagawa Y, Udagawa H (1999) Drag reduction of Newtonian fluid in a circular pipe with a highly water-repellent wall. J Fluid Mech 381:225–238

Woolford B, Maynes D, Webb B (2009) Liquid flow through microchannels with grooved walls under wetting and superhydrophobic conditions. Microfluid Nanofluid 7(1):121–135

Xu M, Sun G, Kim CJ (2014) Infinite lifetime of underwater superhydrophobic states. Phys Rev Lett 113:136103

Yamada T, Hong C, Gregory OJ, Faghri M (2011) Experimental investigations of liquid flow in rib-patterned microchannels with different surface wettability. Microfluid Nanofluid 11:45–55